NOTE

Numerical Solution of the Poroviscoelastic Wave Equation on a Staggered Mesh

José M. Carcione* and Hans B. Helle†

*Osservatorio Geofisico Sperimentale, P.O. Box 2011 Opicina, 34016 Trieste, Italy; and
†Norsk Hydro a.s., E & P Research Centre, N-5020 Bergen, Norway
E-mail: jcarcione@ogs.trieste.it and hans.b.helle@nho.hydro.com

1. INTRODUCTION

Computation of the spatial derivatives with non-local differential operators, such as the Fourier pseudospectral method, may cause strong numerical artifacts in the form of non-causal ringing. This situation occurs when regular grids are used. The problem is attacked by using a staggered pseudospectral technique. The nature and the causes of acausal ringing in regular grid methods and the reasons why staggered grid methods eliminate this problem are explained in the papers by Fornberg [7] and Özdenvar and McMechan [8]. Thus, the objective here is not to propose a new method, but to develop the algorithm for the poroviscoelastic wave equation [3]. Özdenvar and McMechan [9] developed a pseudospectral staggered-grid algorithm for the poroelastic differential equations expressed in the displacement formulation. Here, the equations are expressed in the velocity–stress formulation, including attenuation mechanisms due to fluid/matrix interactions. As is well known, one of the advantages of using the velocity–stress differential equations is the avoidance of the differentiation of the material properties, which eliminates numerical artifacts and makes the algorithm more stable [11].

The algorithm is illustrated for a physical situation that requires very high accuracy, such as the gas–water contact in a natural gas reservoir, where large contrasts in material properties occur. The staggered-grid solution is noise-free in the dynamic range where regular grids generate artifacts that may have amplitudes similar to those of physical arrivals.

2. POROVISCOELASTIC EQUATIONS OF MOTION

The constitutive equations for an inhomogeneous, isotropic poroelastic medium under plane strain conditions are given by [1, 2]

$$\tau_{xx,t} = E v_{x,x} + (E - 2\mu) v_{z,z} + \alpha M \epsilon + s_x, \tag{1}$$

$$\tau_{zz,t} = (E - 2\mu) v_{x,x} + E v_{z,z} + \alpha M \epsilon + s_z, \tag{2}$$

$$\tau_{xz,t} = \mu (v_{x,z} + v_{z,x}) + s_{xz}, \tag{3}$$

$$p_{,t} = -M\epsilon + s_f, \tag{4}$$

and

$$\epsilon = \alpha (v_{x,x} + v_{z,z}) + q_{x,x} + q_{z,z}, \tag{5}$$

where τ_{xx}, τ_{zz}, and τ_{xz} are the total stress components, p is the fluid pressure, the v's and the q's are the solid and fluid (relative to the solid) particle velocities, and s_x, s_z, s_{xz}, and s_f are the external sources of stress, for the solid and the fluid, respectively. The subscript x denotes $\partial/\partial x$.

The elastic coefficients are given by

$$E = K_m + \frac{4}{3}\mu, \tag{6}$$

$$M = \frac{K_s^2}{D - K_m}, \tag{7}$$

$$D = K_s \left[1 + \phi \left(K_s K_f^{-1} - 1 \right) \right], \tag{8}$$

and

$$\alpha = 1 - \frac{K_m}{K_s}, \tag{9}$$

with K_m, K_s, and K_f the bulk moduli of the drained matrix, the solid, and the fluid, respectively; ϕ is the porosity, and μ is the shear modulus of the matrix (drained and saturated). The stiffness E is the P-wave modulus of the dry skeleton, M is the coupling modulus between the solid and the fluid, and α is the poroelastic coefficient of effective stress.

Viscoelasticity is introduced into Biot's poroelastic equations for modeling a variety of dissipation mechanisms related to the skeleton–fluid interaction. One of these mechanism is the squirt-flow [1], by which a force applied to the area of contact between two grains produces a displacement of the surrounding fluid in and out of this area. Since the fluid is viscous, the motion is not instantaneous and energy dissipation occurs. Skeleton–fluid mechanisms are modeled by generalizing the coupling modulus M to a time dependent relaxation function. On the other hand, we assume that E and μ are frequency independent. The approach is explained in [3].

The poroviscoelastic equations of motion are [3]:

(i) Biot–Newton dynamical equations:

$$\tau_{xx,x} + \tau_{xz,z} = \rho v_{x,t} + \rho_f q_{x,t}, \tag{10}$$

$$\tau_{xz,x} + \tau_{zz,z} = \rho v_{z,t} + \rho_f q_{z,t}, \tag{11}$$

where

$$\rho = (1 - \phi)\rho_s + \phi\rho_f$$

is the composite density, with ρ_s and ρ_f the solid and fluid densities, respectively.

(ii) Dynamic Darcy's law:

$$-p_{,x} = \rho_f v_{x,t} + mq_{x,t} + \frac{\eta}{\kappa}q_x, \tag{12}$$

and

$$-p_{,z} = \rho_f v_{z,t} + mq_{z,t} + \frac{\eta}{\kappa}q_z, \tag{13}$$

where $m = T\rho_f/\phi$, with T the tortuosity, η is the fluid viscosity, and κ is the permeability of the medium.

(iii) Constitutive equations:

$$\tau_{xx,t} = Ev_{x,x} + (E - 2\mu)v_{z,z} + \alpha\left(M\epsilon + \sum_{l=1}^{L} e_l\right) + s_x, \tag{14}$$

$$\tau_{zz,t} = (E - 2\mu)v_{x,x} + Ev_{z,z} + \alpha\left(M\epsilon + \sum_{l=1}^{L} e_l\right) + s_z, \tag{15}$$

$$\tau_{xz,t} = \mu(v_{x,z} + v_{z,x}) + s_{xz}, \tag{16}$$

and

$$p_{,t} = -\left(M\epsilon + \sum_{l=1}^{L} e_l\right) + s_f, \tag{17}$$

where $e_l, l = 1, \ldots, L$, are memory variables.

(iv) Memory variable equations:

$$e_{l,t} = -\frac{1}{\tau_{\sigma l}}\left[M\left(L + \sum_{m=1}^{L} \varphi_m\right)^{-1}\varphi_l\epsilon + e_l\right], \tag{18}$$

for $l = 1, \ldots, L$, where $\tau_{\epsilon l}$ and $\tau_{\sigma l}$ are sets of relaxation times, L is the number of attenuation mechanisms, and

$$\varphi_l = \frac{\tau_{\epsilon l}}{\tau_{\sigma l}} - 1. \tag{19}$$

3. STAGGERED MESH AND CALCULATION OF THE SPATIAL DERIVATIVES

On a regular grid the field components and material properties are represented at each grid point, say, represented by the symbol ♠, while on a staggered grid, variables and material

properties are also defined at half-grid points as indicated in the mesh
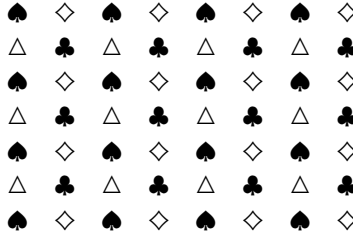
such that

$$
\begin{array}{lll}
\spadesuit \ (i, j) & \tau_{xx}, \tau_{zz}, p, e_l, E, \mu, \alpha, M, \tau_{\sigma l}, \varphi_l, s_x, s_z, s_f, \\
\diamond \ (i + \tfrac{1}{2}, j) & v_x, q_x, \rho, \rho_f, T, \phi, \eta/\kappa, \\
\triangle \ (i, j + \tfrac{1}{2}) & v_z, q_z, \rho, \rho_f, T, \phi, \eta/\kappa, \\
\clubsuit \ (i + \tfrac{1}{2}, j + \tfrac{1}{2}) & \tau_{xz}, \mu, s_{xz}.
\end{array}
\tag{20}
$$

Material properties at half-grid points $\diamond$, $\clubsuit$, and $\triangle$ are computed by averaging the values defined at regular points $\spadesuit$. The averaging is chosen in such a way as to reduce the error between the numerical solution corresponding to an interface aligned with the numerical grid and the equivalent solution obtained with a regular grid. Minimum ringing amplitudes for the example illustrated in the next section are obtained when the averages are computed as follows: the densities, T, ϕ, and η/κ at points $\diamond$ and $\triangle$ as

$$
a^{i+\frac{1}{2}, j} = \tfrac{1}{2}(a^{i,j} + a^{i+1,j})
\tag{21}
$$

and

$$
a^{i, j+\frac{1}{2}} = \tfrac{1}{2}(a^{i,j} + a^{i,j+1}),
\tag{22}
$$

respectively, and μ at points $\clubsuit$ as [10]

$$
\left(\mu^{i+\frac{1}{2}, j+\frac{1}{2}}\right)^{-1} = \tfrac{1}{4}[(\mu^{i,j})^{-1} + (\mu^{i+1,j})^{-1} + (\mu^{i,j+1})^{-1} + (\mu^{i+1,j+1})^{-1}].
\tag{23}
$$

A review of the artifacts and numerical instabilities caused by the Fourier differential operator when using a regular grid can be found in [8]. As the authors show, the use of a staggered grid overcomes these problems. The first-order derivative computed with the staggered differential operator is evaluated between grid points and uses even-based Fourier transforms. The standard first-order differential operator along the x-direction is

$$
D_x\phi = \sum_{k_x=0}^{k_x(N)} ik_x\tilde{\phi}(k_x) \exp(ik_x x),
\tag{24}
$$

where $\tilde{\phi}$ is the Fourier transform of ϕ and $k_x(N)$ is the Nyquist wavenumber. Staggered operators, which evaluate the derivatives between grid points, are given by

$$
D_x^{\pm}\phi = \sum_{k_x=0}^{k_x(N)} ik_x \exp(\pm ik_x \Delta x/2)\tilde{\phi}(k_x) \exp(ik_x x),
\tag{25}
$$

where Δx is the grid spacing.

The staggered poroviscoelastic equations can be written as

$$\diamond \quad D_x^+ \tau_{xx} + D_z^- \tau_{xz} = \rho v_{x,t} + \rho_f q_{x,t},$$

$$\triangle \quad D_x^- \tau_{xz} + D_z^+ \tau_{zz} = \rho v_{z,t} + \rho_f q_{z,t},$$

$$\diamond \quad -D_x^+ p = \rho_f v_{x,t} + m q_{x,t} + \frac{\eta}{\kappa} q_x,$$

$$\triangle \quad -D_z^+ p = \rho_f v_{z,t} + m q_{z,t} + \frac{\eta}{\kappa} q_z,$$

$$\spadesuit \quad \tau_{xx,t} = E D_x^- v_x + (E - 2\mu) D_z^- v_z + \alpha \left(M\epsilon + \sum_{l=1}^{L} e_l \right) + s_x,$$

$$\spadesuit \quad \tau_{zz,t} = (E - 2\mu) D_x^- v_x + E D_z^- v_z + \alpha \left(M\epsilon + \sum_{l=1}^{L} e_l \right) + s_z, \qquad (26)$$

$$\clubsuit \quad \tau_{xz,t} = \mu (D_z^+ v_x + D_x^+ v_z) + s_{xz},$$

$$\spadesuit \quad p_{,t} = -\left(M\epsilon + \sum_{l=1}^{L} e_l \right) + s_f,$$

$$\spadesuit \quad e_{l,t} = -\frac{1}{\tau_{\sigma l}} \left[M \left(L + \sum_{m=1}^{L} \varphi_m \right)^{-1} \varphi_l \epsilon + e_l \right],$$

$$\spadesuit \quad \epsilon = \alpha (D_x^- v_x + D_z^- v_z) + D_x^- q_x + D_z^- q_z.$$

A time splitting algorithm is used to solve the differential equations. The technique, which has fourth-order accuracy in time, is illustrated in detail in [4, 5].

TABLE I
Material Properties of the Single Constituents

Solid	
Bulk modulus, K_s	35 GPa
Density, ρ_s	2650 kg/m³
Matrix	
Bulk modulus, K_m	1.7 GPa
Shear modulus, μ	1.855 GPa
Porosity, ϕ	0.3
Permeability, κ	1 D
Tortuosity, T	1
Gas	
Bulk modulus, K_g	0.022 GPa
Density, ρ_g	100 kg/m³
Viscosity, η_g	0.015 cP
Water	
Bulk modulus, K_w	2.4 GPa
Density, ρ_w	1000 kg/m³
Viscosity, η_w	1 cP

4. EXAMPLE

A gas–water contact generates the characteristic bright spots observed in seismic surveys in the Gulf of Mexico. This is one situation where the differential operator introduces a non-causal ringing noise, generated by discontinuities in the material properties. We consider the same media as those in the plane-wave analysis by Dutta and Ode [6], who computed the reflection coefficients for a gas–water contact. In addition, we introduce a squirt-flow
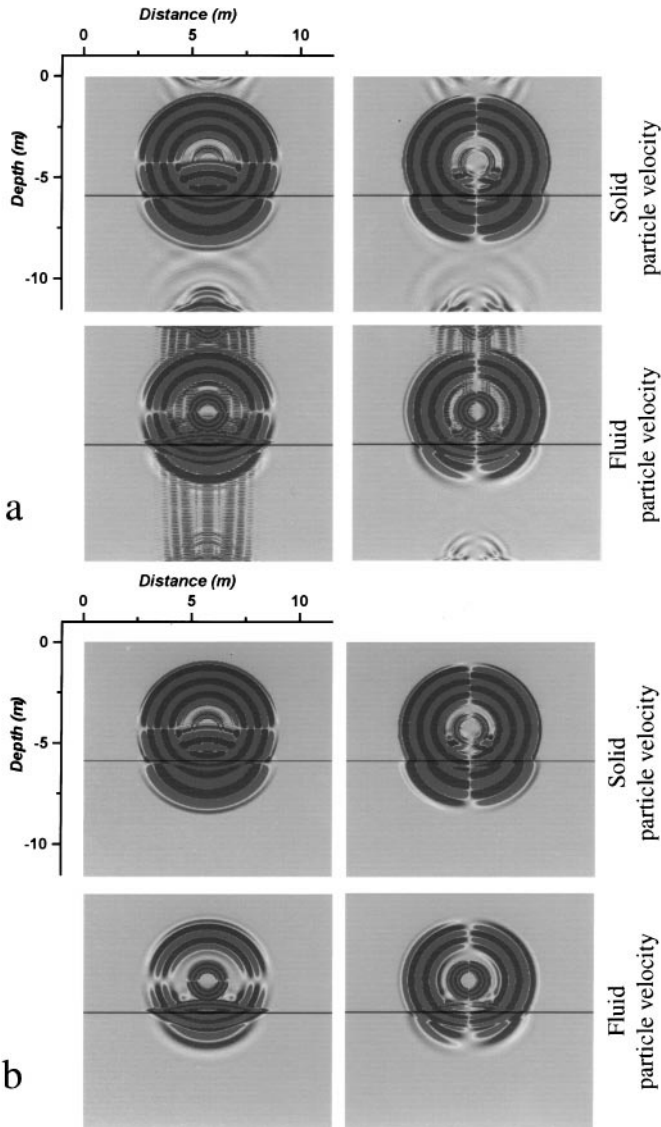

FIG. 1. Snapshots after 2.25 ms of the solid and fluid particle velocities on a regular grid (a) and a staggered grid (b). A bulk source, with a central frequency of 2.1 kHz, is at 1.5 m above the gas–water interface. No absorbing boundaries have been applied since the wavefield does not reach the boundary of the mesh. The staggered differential operator (b) does not generate the strong ringing and acausal noise observed in the regular-grid snapshots (a).

CARCIONE AND HELLE

TABLE II
Properties of the Saturated Rock

	Water-filled	Gas-filled
ρ	2155 kg/m³	1885 kg/m³
$c_{P_+}(0)$	2081 m/s	1500 m/s
$c_{P_+}(\infty)$	2234 m/s	1506 m/s
$c_{P_-}(0)$	937 m/s	467 m/s
$c_{P_-}(\infty)$	971 m/s	467 m/s
$f_{\text{peak}}(P_+)$	3.22 kHz	8.07 kHz
$\alpha_{P_+}(f_{\text{peak}})$	0.8 dB	0.116 dB

dissipation mechanism as in [3]. The material properties of the single constituents and saturated porous medium are given in Tables I and II, respectively. Table II gives the relaxed ($\omega = 0$) and unrelaxed ($\omega = \infty$) phase velocities of the fast compressional wave (c_{P_+}) and the slow wave (c_{P_-}), the central frequency of the dominant attenuation peak (f_{peak}) corresponding to the squirt flow in water-saturated sandstone and to the Biot peak in gas-saturated sandstone, and the attenuation factor at the central frequency (α_{P_+}). Phase velocities and attenuations are plotted in Dutta and Ode's article, together with the reflection and transmission coefficients.

We consider a regular grid of 231×231 points and a staggered grid of 238×238 points, both with a grid spacing of 5 cm. The source is a Ricker-type wavelet with dominant frequency of 2.1 kHz applied to the bulk. The wavefield is computed with a time step of 2.5 μs. Figures 1a and 1b compare snapshots at 2.25 ms caused by a source located at 1.5 m above the gas–water contact. The wave fronts are represented by circles or segments of circles. No absorbing boundaries have been applied since, in the present simulation, the
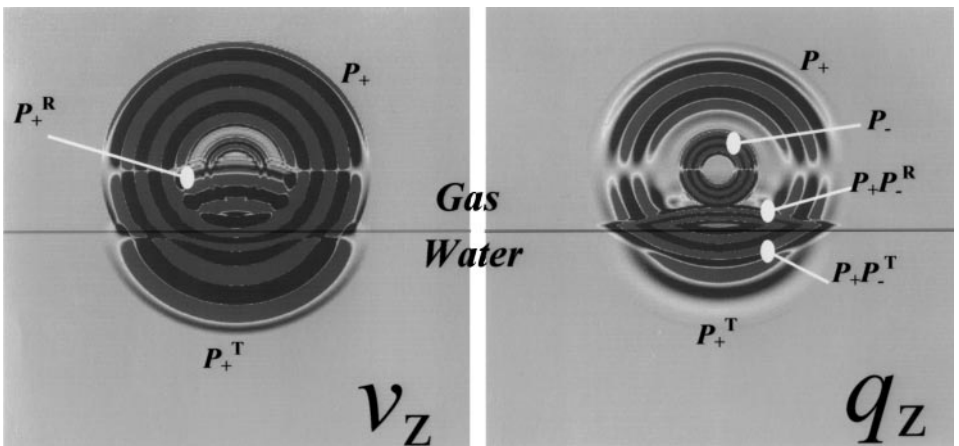

FIG. 2. Interpretation of the individual wave events in the snapshots of vertical displacement velocity of the solid (left) and the fluid (right). Four events can be observed in the upper gas-filled rock: the fast P-wave (P_+), the reflected P-wave (P_+^R), the direct slow P-wave (P_-), and another slow P-wave ($P_+P_-^R$) attached to the contact boundary. In the lower water-filled rock the transmitted fast P-wave (P_+^T) is attenuated by the squirt-flow mechanism. On both sides of the gas/fluid contact significant slow waves are generated by conversion of the fast P-wave. Note that the velocity of the slow wave in the water zone is about twice that in the gas zone (see Table II).

wavefield does not reach the boundary of the mesh. As can be appreciated, the staggered differential operator does not generate the strong ringing and acausal noise observed in the regular-grid snapshots.

The individual wave types are identified in Fig. 2. Four different events can be clearly identified in the upper medium (gas-filled pores) and two events in the lower medium. In the lower medium (water-filled pores) the fast P-wave is strongly attenuated by the squirt-flow mechanism. On both sides of the gas/fluid contact significant slow waves are generated by conversion of the fast P-wave. The latter is considered to be an important mechanism for the loss of fast P-wave energy in the sedimentary layers [3].

ACKNOWLEDGMENTS

REFERENCES

1. M. A. Biot, Mechanics of deformation and acoustic propagation in porous media, *J. Appl. Phys.* **33**, 1482 (1962).

2. M. A. Biot and D. G. Willis, The elastic coefficients of the theory of consolidation, *J. Appl. Mech.* **24**, 594 (1957).

3. J. M. Carcione, Viscoelastic effective rheologies for modeling wave propagation in porous media, *Geophys. Prospect.* **46**, 249 (1998).

4. J. M. Carcione, Wave propagation in anisotropic, saturated porous medium: Plane-wave theory and numerical simulation, *J. Acoust. Soc. Am.* **99**(5), 2655 (1996).

5. J. M. Carcione and G. Quiroga Goode, Some aspects of the physics and numerical modeling of Biot compressional waves, *J. Comput. Acoustics* **3**(4), 261 (1995).

6. N. C. Dutta and H. Ode, Seismic reflections from a gas–water contact, *Geophysics* **48**, 148 (1983).

7. B. Fornberg, High-order finite differences and pseudo-spectral method on staggered grids, *SIAM J. Numer. Anal.* **27**, 904 (1990).

8. T. Özdenvar and G. McMechan, Causes and reduction of numerical artifacts in pseudo-spectral wavefield extrapolation, *Geophys. J. Int.* **126**, 819 (1996).

9. T. Özdenvar and G. McMechan, Algorithms for staggered-grid computations for poroelastic, elastic, acoustic, and scalar wave equations, *Geophys. Prospect.* **45**, 403 (1997).

10. T. Røsten, L. Amundsen, B. Arnsten, and Å. Kristensen, Finite-difference modelling with application to interface wave propagation, in *Proceedings, Third International Conference on Underwater Acoustics*, edited by Papadakis (1996), p. 315.

11. J. Virieux, P–SV wave propagation in heterogeneous media: Velocity–stress finite difference method, *Geophysics* **51**, 889 (1986).